Three-Dimensional Surface Reconstruction From Multistatic SAR Images

Brian D. Rigling, *Member, IEEE,* and Randolph L. Moses, *Senior Member, IEEE*

Abstract—This paper discusses reconstruction of three-dimensional surfaces from multiple bistatic synthetic aperture radar (SAR) images. Techniques for surface reconstruction from multiple monostatic SAR images already exist, including interferometric processing and stereo SAR. We generalize these methods to obtain algorithms for bistatic interferometric SAR and bistatic stereo SAR. We also propose a framework for predicting the performance of our multistatic stereo SAR algorithm, and, from this framework, we suggest a metric for use in planning strategic deployment of multistatic assets.

Index Terms—Bistatic, ground map, surface reconstruction, synthetic aperture radar (SAR), three-dimensional (3-D).

I. INTRODUCTION

RECENT developments in unmanned aerial vehicle (UAV) technology is spurring new interest in the fields of bistatic and multistatic synthetic aperture radar (SAR) [1]–[8]. A low-cost UAV may be teamed with a high-power transmitter at a safe standoff distance to conduct passive ground surveillance using bistatic SAR. Receiving platforms may also exploit illuminators of opportunity including overpassing satellites and local commercial broadcasters.

Several authors have considered bistatic SAR image formation (see, e.g., [9]–[12]). Soumekh [11], [13] suggests using multiple receiving platforms with a single transmitting platform to form a multistatic system. A multistatic system can be used to form a set of bistatic images. Additionally, the multiple bistatic images can be coherently or incoherently combined to form a three-dimensional (3-D) reconstruction of the imaged scene.

Earlier works involving multiple monostatic apertures have illustrated methods for height estimation, including interferometric SAR [14]–[16] and stereo SAR [17], [18]. Interferometric SAR typically involves coherent processing of a pair of images formed from data collected by two separate antennas on the same data collection platform and has proven to be effective at forming topographic ground maps of smoothly varying terrain. Stereo SAR requires two or more images formed by platforms separated in aspect angle. Height estimates are obtained by measuring the layover differences between the images [19], [20]. High-resolution SAR systems that are becoming available will improve the performance of both algorithms in estimating

the height of complex target substructures. As we will show, monostatic stereo techniques can be generalized for application to images created by a multistatic system, incorporating multiple transmitting and receiving platforms, and interferometric techniques may be applied to a pair of bistatic SAR images, formed by a receiver equipped with two or more antennas.

This paper develops the theory required for performing 3-D surface reconstruction using a multistatic SAR system. We derive the theory necessary for interferometric processing of two bistatic SAR images to obtain height estimates, and we propose an algorithm which implements stereo processing of two or more bistatic images. Our results generalize existing monostatic SAR algorithms. We provide a framework for predicting the performance of the stereo SAR algorithm, and based on this framework, we propose strategies for coordinating the receiving platforms used in a multistatic system.

An outline of the paper is as follows. In Section II, we state our model for bistatic phase history data collection and bistatic SAR image formation. Based on these models, we illustrate how 3-D point scatterers are projected into a two-dimensional (2-D) bistatic SAR image. This projection is commonly known as layover. In Section III, we derive and demonstrate interferometric processing of a pair of registered bistatic SAR images. In Section IV, we generalize monostatic stereo SAR processing to develop an algorithm which estimates the heights of surfaces in a scene, based on the difference in layover between two bistatic images formed at different look angles. In Section V, we extend the stereo SAR concept to consider more than two bistatic apertures, and we provide a framework for predicting the performance of this algorithm. Our performance prediction framework allows us to suggest strategies for coordinating multistatic SAR systems. Finally, in Section VI, we state our conclusions and outline areas of future work.

II. BISTATIC PHASE HISTORY DATA

Consider the bistatic SAR data collection geometry shown in Fig. 1. The center of the scene to be imaged is located at the origin of coordinates, and the ground plane is the x–y plane. A scatterer within that scene is located at $\underline{r}_m = (x_m, y_m, z_m)$. At a given time τ, the location of the transmitter is $\underline{r}_t(\tau) = (x_t(\tau), y_t(\tau), z_t(\tau))$, and the location of the receiver is $\underline{r}_r(\tau) = (x_r(\tau), y_r(\tau), z_r(\tau))$.

As the transmitter moves along its flight path, the radiating antenna periodically transmits pulses of energy in the direction of the scene center. We assume that transmitted pulses have uniform power over the frequency range $f \in [f_0, f_0 + B]$, where f_0 and B represent the initial frequency and bandwidth of the transmitted pulse, respectively. Each transmitted pulse travels
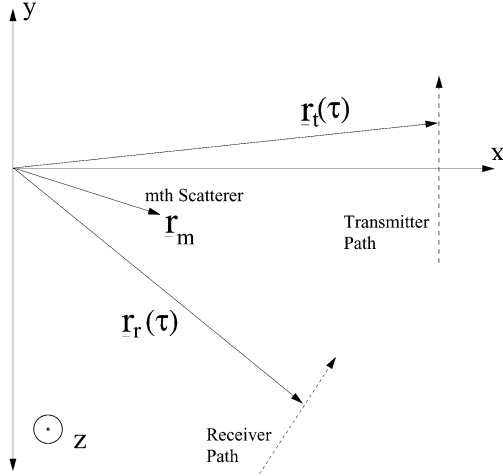
Fig. 1. Top view of a bistatic data collection geometry. The x–y plane is the ground plane.

from the transmitter to the scene of interest, where it is reflected by scatterers within the area of illumination. Some of these reflected signals are observed by the antenna on the receiving platform, and are recorded in the form of phase history data. We model this data in the frequency domain as the sum of the time-delayed returns from all of the scatterers in the scene. This representation for phase history data is consistent with the Fourier transform of compressed pulses, or the output of a dechirp-on-receive (stretch) processor, and is commonly used in derivations of polar format image formation algorithms (see, e.g., [19] and [20]). This model [12] is written as

$$S(f_i, \tau_k) = \sum_m A_m e^{-j2\pi f_i \frac{\Delta R_m(\tau_k)}{c}} + w(f_i, \tau_k) \qquad (1)$$

where the sampled frequencies f_i are spaced over $[f_0, f_0 + B]$, and the sampled times τ_k are spaced over $[-T/2, T/2]$. The signal is corrupted by white Gaussian noise, represented by $w(f_i, \tau_k)$. The complex scattering coefficient of the mth scattering center is represented by A_m. The time delay of the response from the mth scattering center is equal to the bistatic differential range of that scatterer $\Delta R_m(\tau_k)$ divided by the speed of light c. In the far-field, the bistatic differential range is well approximated [12] by

$$
\begin{aligned}
\Delta R_m(\tau_k) \approx &-x_m \cos \phi_t(\tau_k) \cos \theta_t(\tau_k) \\
&- y_m \sin \phi_t(\tau_k) \cos \theta_t(\tau_k) - z_m \sin \theta_t(\tau_k) \\
&- x_m \cos \phi_r(\tau_k) \cos \theta_r(\tau_k) \\
&- y_m \sin \phi_r(\tau_k) \cos \theta_r(\tau_k) - z_m \sin \theta_r(\tau_k) \quad (2)
\end{aligned}
$$

where the variables $\phi_t(\tau)$ and $\phi_r(\tau)$ ($\theta_t(\tau)$ and $\theta_r(\tau)$) denote the azimuth (elevation) angles of the transmitter and receiver, with respect to the scene center at slow time τ.

Based on (1) and (2), one may form an image by assuming a scatterer is located at the center of each pixel and then independently calculating the maximum likelihood estimate of each scatterer's reflectivity. Thus, a ground-plane image ($z = 0$) may be formed by applying the matched filter [see (3), shown at the bottom of the page] to the phase history data for each (x, y) pixel location.

We remark that the differential range in (2) is subject to errors caused by mis-measurement of the transmitter and receiver positions. We assume that the phase errors induced by these discrepancies, as well as phase errors from other sources, may be corrected to within a linear phase function, resulting in an unknown shift $(\tilde{x}, \tilde{y})$ of the final image. Techniques for correcting bistatic motion measurement errors are described in [21] and [22].

In (1) and (2), the (x, y, z) location of each scatterer is encoded in the observed differential range $\Delta R_m(\tau)$ of that scatterer. However, the matched filter (3) used in image formation assumes that all scatterers lie on the ground plane, thus implying that a projection takes place in the image formation process. To understand the nature of this projection, we will apply further approximations to our expression for the bistatic differential range. We first assume that the ground range and slant range of the transmitter, $r_t = \sqrt{x_t(\tau)^2 + y_t(\tau)^2}$ and $R_t = \sqrt{x_t(\tau)^2 + y_t(\tau)^2 + z_t(\tau)^2}$, are sufficiently large such that they may be treated as constants with respect to slow time τ. We make the same assumption about the ground range and slant range of the receiver, $r_r = \sqrt{x_r(\tau)^2 + y_r(\tau)^2}$ and $R_r = \sqrt{x_r(\tau)^2 + y_r(\tau)^2 + z_r(\tau)^2}$. Finally, we assume that the transmitter and receiver fly linear flight paths at constant velocities and constant altitudes. The locations of the transmitter and receiver at their aperture midpoints are given by $(\bar{x}_t, \bar{y}_t, \bar{z}_t)$ and $(\bar{x}_r, \bar{y}_r, \bar{z}_r)$, and the transmitter and receiver velocity vectors are (v_{xt}, v_{yt}, v_{zt}) and (v_{xr}, v_{yr}, v_{zr}). Thus, we may approximate $\cos \phi_t(\tau_k)$ with $(\bar{x}_t + v_{xt}\tau_k)/r_t$, $\cos \theta_t(\tau_k)$ with r_t/R_t, etc. This allows the approximate differential range function in (2) to be further approximated by a linear function of slow time

$$
\begin{aligned}
\Delta R_m(\tau_k) \approx &-x_m \frac{\bar{x}_t + v_{xt}\tau_k}{r_t} \frac{r_t}{R_t} - y_m \frac{\bar{y}_t + v_{yt}\tau_k}{r_t} \frac{r_t}{R_t} \\
&- z_m \frac{\bar{z}_t + v_{zt}\tau_k}{R_t} - x_m \frac{\bar{x}_r + v_{xr}\tau_k}{r_r} \frac{r_r}{R_r} \\
&- y_m \frac{\bar{y}_r + v_{yr}\tau_k}{r_r} \frac{r_r}{R_r} - z_m \frac{\bar{z}_r + v_{zr}\tau_k}{R_r} \\
= &-\left[x_m \left(\frac{\bar{x}_t}{R_t} + \frac{\bar{x}_r}{R_r} \right) + y_m \left(\frac{\bar{y}_t}{R_t} + \frac{\bar{y}_r}{R_r} \right) \right. \\
&\left. + z_m \left(\frac{\bar{z}_t}{R_t} + \frac{\bar{z}_r}{R_r} \right) \right] - \left[x_m \left(\frac{v_{xt}}{R_t} + \frac{v_{xr}}{R_r} \right) \right. \\
&\left. + y_m \left(\frac{v_{yt}}{R_t} + \frac{v_{yr}}{R_r} \right) + z_m \left(\frac{v_{zt}}{R_t} + \frac{v_{zr}}{R_r} \right) \right] \tau_k \\
\triangleq &-\beta_0 - \beta_1 \tau_k. \qquad (4)
\end{aligned}
$$

$$s(x, y) = \frac{1}{N_f N_\tau} \sum_{i=1}^{N_f} \sum_{k=1}^{N_\tau} S(f_i, \tau_k) \cdot e^{-j\frac{2\pi f_i}{c}[x(\cos \phi_t(\tau_k) \cos \theta_t(\tau_k) + \cos \phi_r(\tau_k) \cos \theta_r(\tau_k)) + y(\sin \phi_t(\tau_k) \cos \theta_t(\tau_k) + \sin \phi_r(\tau_k) \cos \theta_r(\tau_k))]}$$

$$(3)$$

Equation (4) describes a transformation which relates the linear approximation of the differential range $\Delta R(\tau) = -\beta_0 - \beta_1 \tau$ to the actual location of a scatterer in the scene. This transformation may be written as

$$\begin{bmatrix} \beta_0 \\ \beta_1 \end{bmatrix} = \begin{bmatrix} \frac{\bar{x}_t}{R_t} + \frac{\bar{x}_r}{R_r} & \frac{\bar{y}_t}{R_t} + \frac{\bar{y}_r}{R_r} & \frac{\bar{z}_t}{R_t} + \frac{\bar{z}_r}{R_r} \\ \frac{v_{xt}}{R_t} + \frac{v_{xr}}{R_r} & \frac{v_{yt}}{R_t} + \frac{v_{yr}}{R_r} & \frac{v_{zt}}{R_t} + \frac{v_{zr}}{R_r} \end{bmatrix} \\ \times \begin{bmatrix} x_m \\ y_m \\ z_m \end{bmatrix} \triangleq Q \begin{bmatrix} x_m \\ y_m \\ z_m \end{bmatrix}. \quad (5)$$

In contrast, the image formation process implicitly assumes that scatterers are located on the ground plane $(z = 0)$, and, thus, defines a transformation

$$\begin{bmatrix} \hat{x}_m \\ \hat{y}_m \end{bmatrix} = \begin{bmatrix} \frac{\bar{x}_t}{R_t} + \frac{\bar{x}_r}{R_r} & \frac{\bar{y}_t}{R_t} + \frac{\bar{y}_r}{R_r} \\ \frac{v_{xt}}{R_t} + \frac{v_{xr}}{R_r} & \frac{v_{yt}}{R_t} + \frac{v_{yr}}{R_r} \end{bmatrix}^{-1} \\ \times \begin{bmatrix} \beta_0 \\ \beta_1 \end{bmatrix} \triangleq P \begin{bmatrix} \beta_0 \\ \beta_1 \end{bmatrix} \quad (6)$$

relating the linear approximation of the differential range to an (x, y) pixel location. It is at this approximate pixel location $(\hat{x}_m, \hat{y}_m)$ that a point response will appear, corresponding to the original scatterer located at (x_m, y_m, z_m). Thus, using (5) and (6), we define the linear operation that projects 3-D point scatterers into a 2-D image as

$$\begin{bmatrix} \hat{x}_m \\ \hat{y}_m \end{bmatrix} = PQ \begin{bmatrix} x_m \\ y_m \\ z_m \end{bmatrix}. \quad (7)$$

Note that if $\bar{z}_t = \bar{z}_r = v_{zt} = v_{zr} = 0$, then $PQ = \begin{bmatrix} I & 0 \end{bmatrix}$ and scatterers project vertically onto a ground-plane image. The SAR imaging phenomenon represented by the projection operation in (7), wherein 3-D scattering center locations are projected into the 2-D SAR image, is commonly known as layover [19], [20]. Equation (7) forms the basis of both the interferometric and the stereo height estimation techniques developed in the next two sections.

III. BISTATIC INTERFEROMETRIC SAR

A. Theory

We now consider a bistatic interferometric system involving a transmitting platform and a single receiving platform equipped with two physically separated receiving antennas. This allows formation of two coherent bistatic SAR images, one from the phase history data from each receiving antenna. The differences between these two images, caused by the physical separation of the receiving antennas, allows height estimation to be accomplished interferometrically. Given the geometric configuration of the bistatic system, we can compute the projection matrices for the two bistatic apertures; then, the ideal layover in each image due to a scatterer height of 1 m is

$$\begin{bmatrix} \Delta x_{mi} \\ \Delta y_{mi} \end{bmatrix} = P_i Q_i \begin{bmatrix} 0 \\ 0 \\ 1 \end{bmatrix} \quad i = 1, 2 \quad (8)$$

where P_i and Q_i are defined for each of the two receive antennas using (5) and (6). To examine the effect of layover on images formed via matched filtering, we first rewrite (3) as

$$s(x, y) = \frac{1}{N_f N_\tau} \sum_{i=1}^{N_f} \sum_{k=1}^{N_\tau} S(f_i, \tau_k) e^{j \frac{2\pi f_i}{c} \Delta R_{xy}(\tau_k)}$$

$$\approx e^{j \frac{2\pi f_c}{c} \Delta \bar{R}_{xy}} \cdot \frac{1}{N_f N_\tau} \sum_{i=1}^{N_f} \sum_{k=1}^{N_\tau} S(f_i, \tau_k)$$

$$\times e^{j \frac{2\pi \delta_f (i - N_f/2)}{c} \Delta R_{xy}(\tau_k)}$$

$$\approx e^{j \frac{2\pi f_c}{c} \Delta \bar{R}_{xy}} H(x, y) \quad (9)$$

where we have factored out a constant phase shift corresponding to the center frequency f_c of our collected data. The spacing between frequency samples is given by δ_f, and the 2-D differential range function $\Delta R_{xy}(\tau_k)$ is given by (2) with $z_m = 0$. The envelope of the imaged point scatterer is represented by $H(x, y)$, and its phase is given by $\exp\{j(2\pi f_c)/(c) \Delta \bar{R}_{xy}\}$ where $\Delta \bar{R}_{xy}$ is the differential range at the midpoint of the synthetic aperture $(k = N_\tau/2)$.

We now make a narrow-band assumption about our data, assuming that our frequency samples are close to the center frequency $f_c = f_0 + B/2$ and that our samples in slow time are close to $\tau = 0$. Using (4), (8), and (9), we may then approximate the effect of layover on each ground-plane bistatic SAR image as

$$s_1'(x, y) \approx H_1(x - z_m \Delta x_{m1}, y - z_m \Delta y_{m1}) \\ \times \exp\left\{ j \frac{2\pi f_c}{c} z_m \left[\Delta x_{m1} \left(\frac{\bar{x}_t}{R_t} + \frac{\bar{x}_{r1}}{R_{r1}} \right) \right. \right. \\ \left. \left. + \Delta y_{m1} \left(\frac{\bar{y}_t}{R_t} + \frac{\bar{y}_{r1}}{R_{r1}} \right) \right] \right\} \quad (10)$$

$$s_2'(x, y) \approx H_2(x - z_m \Delta x_{m2}, y - z_m \Delta y_{m2}) \\ \times \exp\left\{ j \frac{2\pi f_c}{c} z_m \left[\Delta x_{m2} \left(\frac{\bar{x}_t}{R_t} + \frac{\bar{x}_{r2}}{R_{r2}} \right) \right. \right. \\ \left. \left. + \Delta y_{m2} \left(\frac{\bar{y}_t}{R_t} + \frac{\bar{y}_{r2}}{R_{r2}} \right) \right] \right\} \quad (11)$$

where the response of the mth scatterer is assumed to be dominant at (x, y). Equations (10) and (11) show that the principal effects of a nonzero height are to shift the envelope $H(x, y)$ to the laid over position and to shift the image phase at that position. Given a sufficiently small separation between the two receiving antennas, we now make the following assumptions.

1) $\Delta x_{m1} - \Delta x_{m2}$ is small relative to the image resolution.
2) $\Delta y_{m1} - \Delta y_{m2}$ is small relative to the image resolution.
3) $H(x - z_m \Delta x_{m1}, y - z_m \Delta y_{m1}) = H_1(x - z_m \Delta x_{m1}, y - z_m \Delta y_{m1}) = H_2(x - z_m \Delta x_{m2}, y - z_m \Delta y_{m2})$.
4) $x_{r1} \approx x_{r2}, y_{r1} \approx y_{r2}$ and $R_{r1} \approx R_{r2}$.

These assumption are analogous to those used in monostatic IFSAR. The product of the first image and the complex

conjugate of the second image may, thus, be approximated as

$$
\begin{aligned}
C(x,y) &= s_1'(x,y)\overline{s_2'(x,y)} \\
&\approx |H(x,y)|^2 \exp\Big\{ j\frac{2\pi}{\lambda_c} z_m \left[(\Delta x_{m1} - \Delta x_{m2}) \right. \\
&\quad \times \left(\frac{\bar{x}_t}{R_t} + \frac{\bar{x}_{r1}}{R_{r1}} \right) + (\Delta y_{m1} - \Delta y_{m2}) \left.\left(\frac{\bar{y}_t}{R_t} + \frac{\bar{y}_{r1}}{R_{r1}} \right) \right] \Big\}
\end{aligned}
\tag{12}
$$

where $\lambda_c = c/f_c$. Examining the phase of $C(x,y)$

$$
\begin{aligned}
\angle C(x,y) = \frac{2\pi z_m}{\lambda_c} &\left[(\Delta x_{m1} - \Delta x_{m2}) \left(\frac{\bar{x}_t}{R_t} + \frac{\bar{x}_{r1}}{R_{r1}} \right) \right. \\
&\left. + (\Delta y_{m1} - \Delta y_{m2}) \left(\frac{\bar{y}_t}{R_t} + \frac{\bar{y}_{r1}}{R_{r1}} \right) \right]
\end{aligned}
\tag{13}
$$

we see that the height of the dominant scatterer in an imaged pixel may be estimated as

$$
\begin{aligned}
z_m = \frac{\lambda_c \angle C(x,y)}{2\pi} &\left[(\Delta x_{m1} - \Delta x_{m2}) \left(\frac{\bar{x}_t}{R_t} + \frac{\bar{x}_{r1}}{R_{r1}} \right) \right. \\
&\left. + (\Delta y_{m1} - \Delta y_{m2}) \left(\frac{\bar{y}_t}{R_t} + \frac{\bar{y}_{r1}}{R_{r1}} \right) \right]^{-1}.
\end{aligned}
\tag{14}
$$

Thus, interferometric height estimates may be computed from two bistatic SAR images by computing the complex product of (12), taking the phase of this product and inserting it into (14). The maximum and minimum unambiguous heights may be calculated by substituting $\angle C(x,y) = \pm\pi$ into (14). Note that the above result is derived based on a point scatterer assumption. Scintillation and decorrelation effects, which are not modeled here, are a significant source of height estimation inaccuracy. A thorough discussion of these topics may be found in [19], [23], and [24].

B. Algorithm

Interferometric SAR processing begins by forming two bistatic SAR images, one from each of the receive antennas. These images may in general suffer from differing geo-location errors, thus requiring image registration to be applied in post-processing. A constant false alarm rate detector [25] is then applied in both images. For each pixel whose amplitude exceeds the detection threshold, the complex product of (12) is computed, and the phase resulting from this product is used in (14) to compute a height estimate for a scatterer which has laid over into that pixel. Given a height estimate, we may also estimate the true (x,y) location of a scatterer by removing the shift due to layover using (7) and (8). Specifically, if a scatterer is observed in the first image at $[\hat{x}_{m1} \quad \hat{y}_{m1}]^T$ and has estimated height $\hat{z}_{12}^{(m)}$, then the true (x,y) location of that scatterer may then be computed as

$$
\begin{bmatrix} \hat{x}_{12}^{(m)} \\ \hat{y}_{12}^{(m)} \end{bmatrix} = \begin{bmatrix} \hat{x}_{m1} \\ \hat{y}_{m1} \end{bmatrix} - P_1 Q_1 \begin{bmatrix} 0 \\ 0 \\ \hat{z}_{12}^{(m)} \end{bmatrix}.
\tag{15}
$$

This calculation is commonly known as ortho-rectification. Equation (15) represents a bistatic generalization of corresponding monostatic ortho-rectification equations found in, e.g., [19] and [20].

To demonstrate, we generated two images of a scene illuminated by a transmitter with a flight path centered on and orthogonal to the positive x axis. A simulated receiving platform was located at an azimuth angle of $\phi_r = -20°$ and observed the scene at broadside with two antenna. The two receiving antenna were given a vertical separation of 10 m. Fig. 2(a) and (b) shows the two bistatic images formed from each receiving antenna; their magnitudes are nearly identical, in keeping with assumptions (A-1)–(A-4) above, and differences in their phases encode scatterer height. All of the scattering centers shown were equal in amplitude, and they were scaled prior to addition of white Gaussian noise in order to yield a peak signal-to-noise ratio (SNR) of 30 dB. The above algorithm was used to coherently process the two images in Fig. 2(a) and (b) to yield height estimates for each point scatterer in the scene. The parameters used in this example are given in Table I. Fusing these height estimates with one of the original images yields the 3-D reconstruction shown in Fig. 2(c). The true locations of the simulated point scatterers are shown in Fig. 2(d). Note that Fig. 2(c) gives height estimates only at the point scatterer locations, due to the pixel-by-pixel processing of IFSAR, and does not give the surface effect that we will see in stereo processing.

C. Performance

The accuracy of interferometric height estimates is typically predicted by assuming an uncertainty in the phase of (12). Here, we assume that this uncertainty, written as

$$
\mathrm{Var}\{\angle C(x,y)\} \triangleq \sigma_\psi^2 = \frac{\sigma^2}{|C(x,y)|^2} + \sigma_s^2
\tag{16}
$$

is dependent on the sum of two components. The first term corresponds to the phase noise induced in each image by the measurement noise represented in (1) by $w(f_i, \tau_k) \sim N(0, \sigma^2)$. The second term σ_s^2 models the phase scintillation observed in SAR images with slightly different look angles. It is expected that σ_s^2 will decrease as Fourier resolution improves. This is based on the assumption that phase scintillation is due in some degree to the interference of multiple scatterers within a resolution cell. The RMS height estimation accuracy expected, given a phase uncertainty of σ_ψ^2, is simply

$$
\begin{aligned}
\sigma_z = \frac{\lambda_c \sigma_\psi}{2\pi} &\left[(\Delta x_{m1} - \Delta x_{m2}) \left(\frac{\bar{x}_t}{R_t} + \frac{\bar{x}_{r1}}{R_{r1}} \right) \right. \\
&\left. + (\Delta y_{m1} - \Delta y_{m2}) \left(\frac{\bar{y}_t}{R_t} + \frac{\bar{y}_{r1}}{R_{r1}} \right) \right]^{-1}.
\end{aligned}
\tag{17}
$$

The images of Fig. 2(a) and (b) contain point scatterers with a signal-to-noise ratio of 30 dB. For each pixel with an SNR above 20 dB, we compared the estimated height of that pixel in Fig. 2(c) to the actual scatterer height, yielding an RMS height estimation accuracy of 30.6 cm. Inserting the parameters shown in Table I into (17) predicts an accuracy of $\sigma_z = 29.3$ centimeters, where σ_s^2 has been assumed to be zero. In practice, both the simulated and predicted performance would be worsened by the effects of scintillation and image decorrelation.
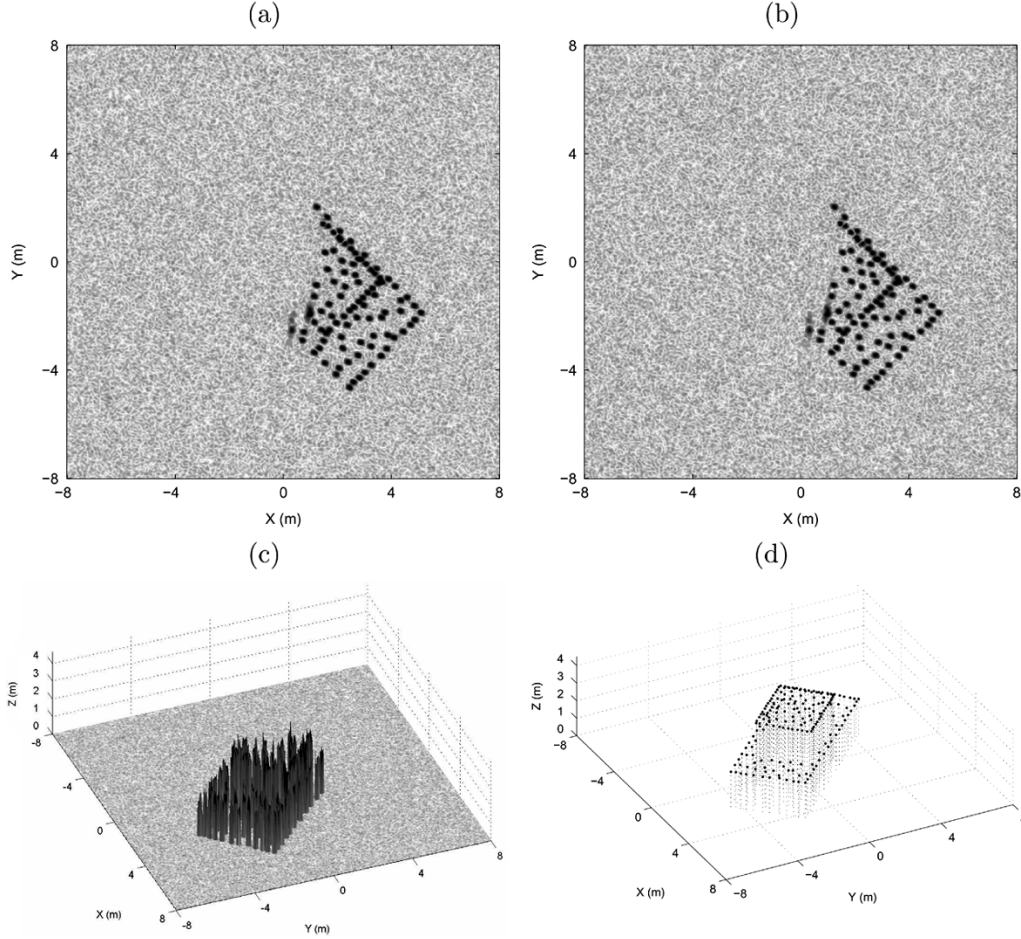
Fig. 2. Transmitter aperture is centered at $\phi_t = 0°$. (a) Image formed by a receiver with aperture centered at $\phi_{r1} = -20°$. (b) An image with an identical envelope formed by a second receiver, displaced 10 m vertically from the first. (c) Topographical image formed interferometrically from the two bistatic images. (d) True locations of the simulated point scatterers. The parameters used to generate this example are given in Table I.

TABLE I
BISTATIC GEOMETRY PARAMETERS CORRESPONDING TO FIG. 2

$\Delta x_{m1} - \Delta x_{m2}$	-0.0613 cm
$\Delta y_{m1} - \Delta y_{m2}$	0.0133 cm
$(\bar{x}_t, \bar{y}_t, \bar{z}_t)$	(30 km, 0 km, 10 km)
$(\bar{x}_{r1}, \bar{y}_{r1}, \bar{z}_{r1})$	(7.5 km, -2.7 km, 3 km)
$(\bar{x}_{r2}, \bar{y}_{r2}, \bar{z}_{r2})$	(7.5 km, -2.7 km, 3.01 km)
λ_c	2.64 cm
σ_ψ	0.081

IV. STEREO HEIGHT ESTIMATION FROM TWO BISTATIC APERTURES

A. Theory

We now consider a system wherein two receiving platforms, each with a single antenna, are teamed with a transmitting platform. The first receiving platform traverses a linear flight path with $(\bar{x}_{r1}, \bar{y}_{r1}, \bar{z}_{r1})$ as its midpoint and $(v_{xr1}, v_{yr1}, v_{zr1})$ as its

velocity vector. Similarly, the flight path of the second receiving platform is defined by $(\bar{x}_{r2}, \bar{y}_{r2}, \bar{z}_{r2})$ and $(v_{xr2}, v_{yr2}, v_{zr2})$. Based on these parameters, we may define projection matrices for the first and second bistatic apertures as

$$Q_i = \begin{bmatrix} \frac{\bar{x}_t}{R_t} + \frac{\bar{x}_{ri}}{R_{ri}} & \frac{\bar{y}_t}{R_t} + \frac{\bar{y}_{ri}}{R_{ri}} & \frac{\bar{z}_t}{R_t} + \frac{\bar{z}_{ri}}{R_{ri}} \\ \frac{v_{xt}}{R_t} + \frac{v_{xri}}{R_{ri}} & \frac{v_{yt}}{R_t} + \frac{v_{yri}}{R_{ri}} & \frac{v_{zt}}{R_t} + \frac{v_{zri}}{R_{ri}} \end{bmatrix}, \quad i = 1, 2 \tag{18}$$

and

$$P_i = \begin{bmatrix} \frac{\bar{x}_t}{R_t} + \frac{\bar{x}_{ri}}{R_{ri}} & \frac{\bar{y}_t}{R_t} + \frac{\bar{y}_{ri}}{R_{ri}} \\ \frac{v_{xt}}{R_t} + \frac{v_{xri}}{R_{ri}} & \frac{v_{yt}}{R_t} + \frac{v_{yri}}{R_{ri}} \end{bmatrix}^{-1}, \quad i = 1, 2. \tag{19}$$

Using (18)–(19), the locations of the mth scatterer in the scene as observed by the first and second receivers, respectively, are

$$\begin{bmatrix} \hat{x}_{m1} \\ \hat{y}_{m1} \end{bmatrix} = P_1 Q_1 \begin{bmatrix} x_m \\ y_m \\ z_m \end{bmatrix} + \begin{bmatrix} \tilde{x}_1 \\ \tilde{y}_1 \end{bmatrix} \tag{20}$$

and

$$\begin{bmatrix} \hat{x}_{m2} \\ \hat{y}_{m2} \end{bmatrix} = P_2 Q_2 \begin{bmatrix} x_m \\ y_m \\ z_m \end{bmatrix} + \begin{bmatrix} \tilde{x}_2 \\ \tilde{y}_2 \end{bmatrix} \tag{21}$$

where the vectors $[\tilde{x}_1 \ \tilde{y}_1]^T$ and $[\tilde{x}_2 \ \tilde{y}_2]^T$ represent shifts in the imaged scene due to uncompensated motion measurement and geo-location errors. We note that a scatterer at a nonzero height

will project differently into the two 2-D images formed from the two bistatic apertures, due to the difference in their layover geometries and their individual platform motion measurement errors. By measuring the difference in this projection, we may estimate a height for that scatterer. We represent the layover offset of the mth scatterer with

$$
\begin{aligned}
\hat{\underline{u}}_m &= \begin{bmatrix} \hat{x}_{m1} \\ \hat{y}_{m1} \end{bmatrix} - \begin{bmatrix} \hat{x}_{m2} \\ \hat{y}_{m2} \end{bmatrix} \\
&= P_1 Q_1 \begin{bmatrix} x_m \\ y_m \\ z_m \end{bmatrix} - P_2 Q_2 \begin{bmatrix} x_m \\ y_m \\ z_m \end{bmatrix} + \begin{bmatrix} \tilde{x}_1 \\ \tilde{y}_1 \end{bmatrix} - \begin{bmatrix} \tilde{x}_2 \\ \tilde{y}_2 \end{bmatrix} \\
&= (P_1 Q_1 - P_2 Q_2) \begin{bmatrix} 0 \\ 0 \\ z_m \end{bmatrix} + \tilde{\underline{u}}_{12} \\
&\triangleq \underline{u}_z z_m + \tilde{\underline{u}}_{12}
\end{aligned}
\tag{22}
$$

where $\tilde{\underline{u}}_{12}$ is the registration error induced between the two images due to their differing motion measurement errors. Furthermore, we do not assume coherency of the image phases for the derivation below, and, in practice, it would be difficult, but not impossible, to maintain image phase coherence across two different platforms.

From (22), we may compute a height estimate for the mth scattering center as

$$
\begin{aligned}
\hat{z}_{12}^{(m)} &= \frac{\underline{u}_z^T \hat{\underline{u}}_m}{\|\underline{u}_z\|^2} = \frac{\underline{u}_z^T (\underline{u}_z z_m + \tilde{\underline{u}}_{12})}{\|\underline{u}_z\|^2} \\
&= z_m + \tilde{z}_{12}.
\end{aligned}
\tag{23}
$$

The lack of perfect geolocation prevents us from recovering an absolute estimate of z_m. However, all of the scatterers in the scene will suffer from the same height estimate offset $\tilde{z}_{12}$. This implies that relative height measurements, between two scattering centers, may still be meaningful. Given a point of reference with a known height, the offset $\tilde{z}_{12}$ may be removed to yield absolute height estimates for each scatterer in the scene.

B. Algorithm

We will now describe an algorithm for performing multistatic stereo SAR height estimation. This implementation faces two impediments. First, it is possible that multiple scatterers of different heights may layover into the same image location, thus complicating one's ability to make accurate observations. Second, scatterers observed in the two images must be correctly associated, and adding to this difficulty, some scatterers may be visible in one image but not the other. To circumvent these complications, we make the following standard assumptions.

B1) Scatterers lie on a surface $h(x,y)$ that is smoothly varying, such that multiple scatterers do not layover into the same image location.

B2) This surface is locally flat.

B3) Multiple scatterers on a locally flat area of this surface may be correctly associated by cross correlation of subimages extracted from the two bistatic images.

Though integral to stereo height estimation algorithms, these assumptions do not always hold in practice, and when violated, some performance loss may result.

Our algorithm for multistatic SAR stereo height estimation is a standard stereo matching technique based on cross correlation, which we briefly describe below. Two bistatic SAR images are formed on the same pixel grid. Given these two images, we first apply a constant false alarm rate detector [25] to the first image to obtain the pixel locations of strong scatterer returns. We then apply a peak finding algorithm, such that out of a cluster of adjacent detections only the pixel with the largest magnitude is returned. This effectively reduces the complexity of the algorithm by limiting the number of detected pixels corresponding to each point scatterer response in the image.

We now iterate through the list of peak detections and attempt to find the shift in location between each detection in the first image and the corresponding return in the second image. To do this, we extract a square subimage, centered about the current peak detection, from the first image, and we extract a larger square subimage, centered about the same pixel location, from the second image. The subimage taken from the first image should be large enough to possess distinct features, which will sufficiently differentiate it from other areas of the scene. The size of the second subimage is determined by the size of the first subimage, the maximum shift expected due to layover differences, and the maximum shift expected due to geo-location errors. We now compute the 2-D cross correlation of the magnitudes of the two subimages. By extracting the location of the peak cross correlation, we obtain the relative shift between the two subimages. After determining relative shifts for all of the peak detections, we compute height estimates using (23) and orthorectify using (15).

The following two examples demonstrate the above algorithm. In the first example, we generated two images of a scene illuminated by a transmitter with a flight path centered on the positive x axis and two receivers located at azimuth angles of $\phi_{r1} = -20°$ and $\phi_{r2} = 5°$. The elevation angles of all three platforms are approximately $20°$, and all three platforms view the scene at broadside. The scene contains 190 point scatterers, configured in the shape of a target. As in the interferometric examples, the amplitude of all of the scattering centers were set equal, and they were scaled before adding white Gaussian noise in order to yield a peak SNR of 30 dB. The two original images both with square 4-in resolution cells are shown in Fig. 3(a) and (b). Note that a lateral separation (in x–y) was maintained between scatterers at different heights. This prevents ambiguities due to overlapping layover, thus artificially satisfying assumption B1).

We applied the above algorithm twice, alternating which image is used as the first image and using 1 meter squared subimages, thus obtaining two sets of height estimates $\{\hat{z}_{12}^{(m)}\}$ and $\{\hat{z}_{21}^{(m)}\}$. Using (15), we then shifted the subimages of the first image to their true locations, as indicated by the $\{\hat{z}_{12}^{(m)}\}$, and shifted the subimages of the second image as indicated by the $\{\hat{z}_{21}^{(m)}\}$. We then averaged the magnitudes of these two height registered images and fused the result with the extracted height estimates. The resulting 3-D reconstruction is shown in Fig. 3(c). The 3-D target reconstruction is fairly accurate, except in areas corresponding to the shadow boundaries of each image. Shadow boundaries were simulated by assigning,
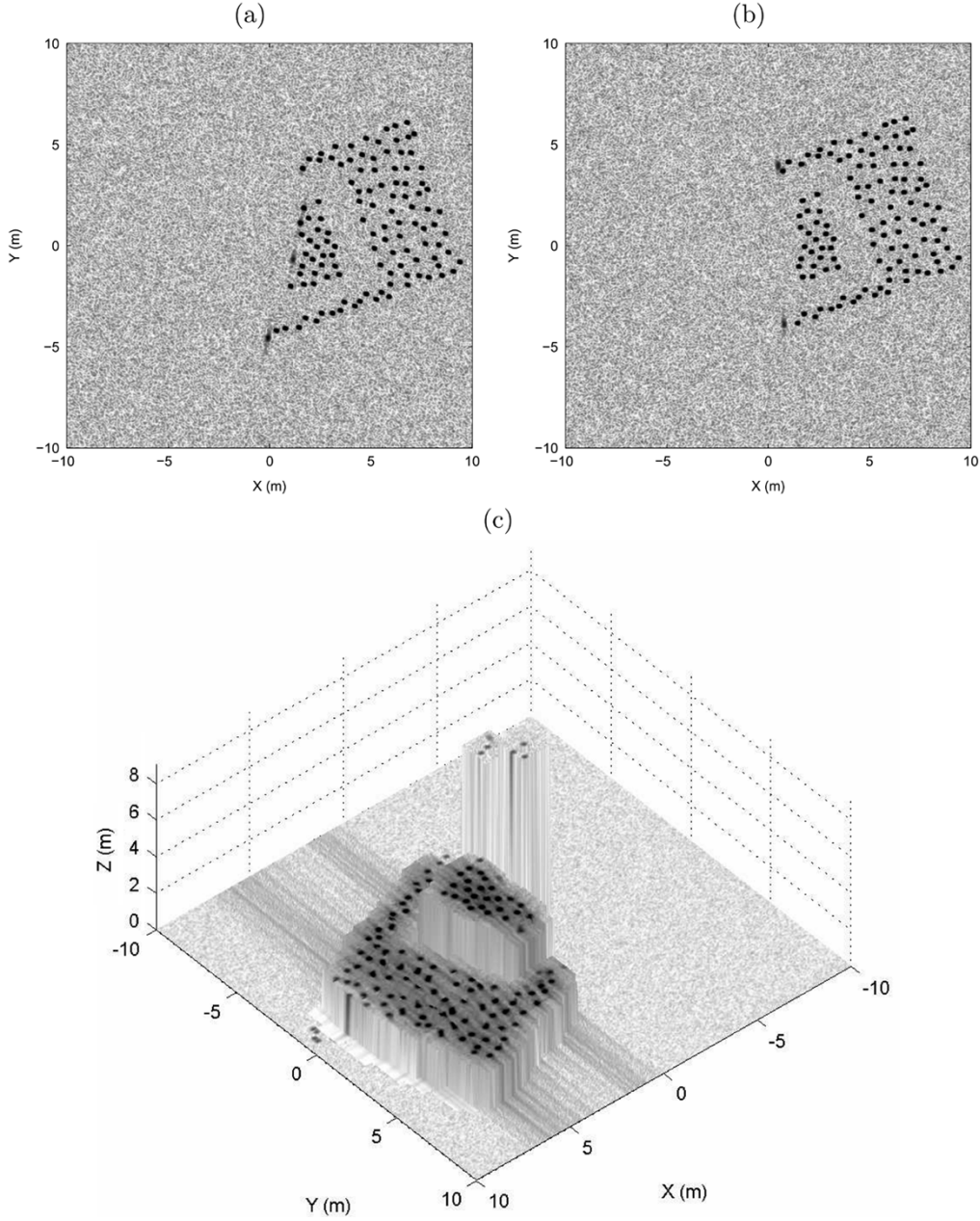
Fig. 3. Transmitter aperture is centered at $\phi_t = 0°$. (a) Image formed by a receiver with aperture centered at $\phi_{r1} = -20°$. (b) Image formed by a receiver with aperture centered at $\phi_{r2} = 5°$. (c) Three-dimensional surface reconstruction formed from (a) and (b). Lateral separation between scatterers at different heights prevents ambiguous height estimates.

on a pulse-by-pulse basis, an amplitude of 1 to scatterers with azimuth angles

$$\phi_m = \arctan\left(\frac{y_m}{x_m}\right) \quad (24)$$

within 90° of the transmitter and receiver look angles, and by assigning an amplitude of 0 to all other scattering centers.

In the second example, the same data collection geometry was implemented, but the simulated scattering centers were arrayed in a tighter configuration in x-y. The second set of example images is shown in Fig. 4(a) and (b), where geometry and scatterer configuration used for the image shown in Fig. 4(a) is identical to that which was used for Fig. 2(a). Stereo processing of these images gives the 3-D reconstruction shown in Fig. 4(c). One

may observe that regions containing scatterers laid over from both simulated heights are subject to greater variance in their height estimates. The accuracy of this reconstruction is lower than that of Fig. 3, but the 3-D shape of the object is still recognizable.

C. Performance

The accuracy of stereo height estimates depends on the geometric configuration of the transmit and receive platforms and also depends on the accuracy of the relative shift estimates between the extracted subimages. Image resolution, scatterer scintillation, subimage decorrelation, and interpolation accuracy all affect the accuracy of the cross correlation. If one assumes that the shift estimates $\{\hat{\underline{u}}_m\}$ have Gaussian errors with zero means
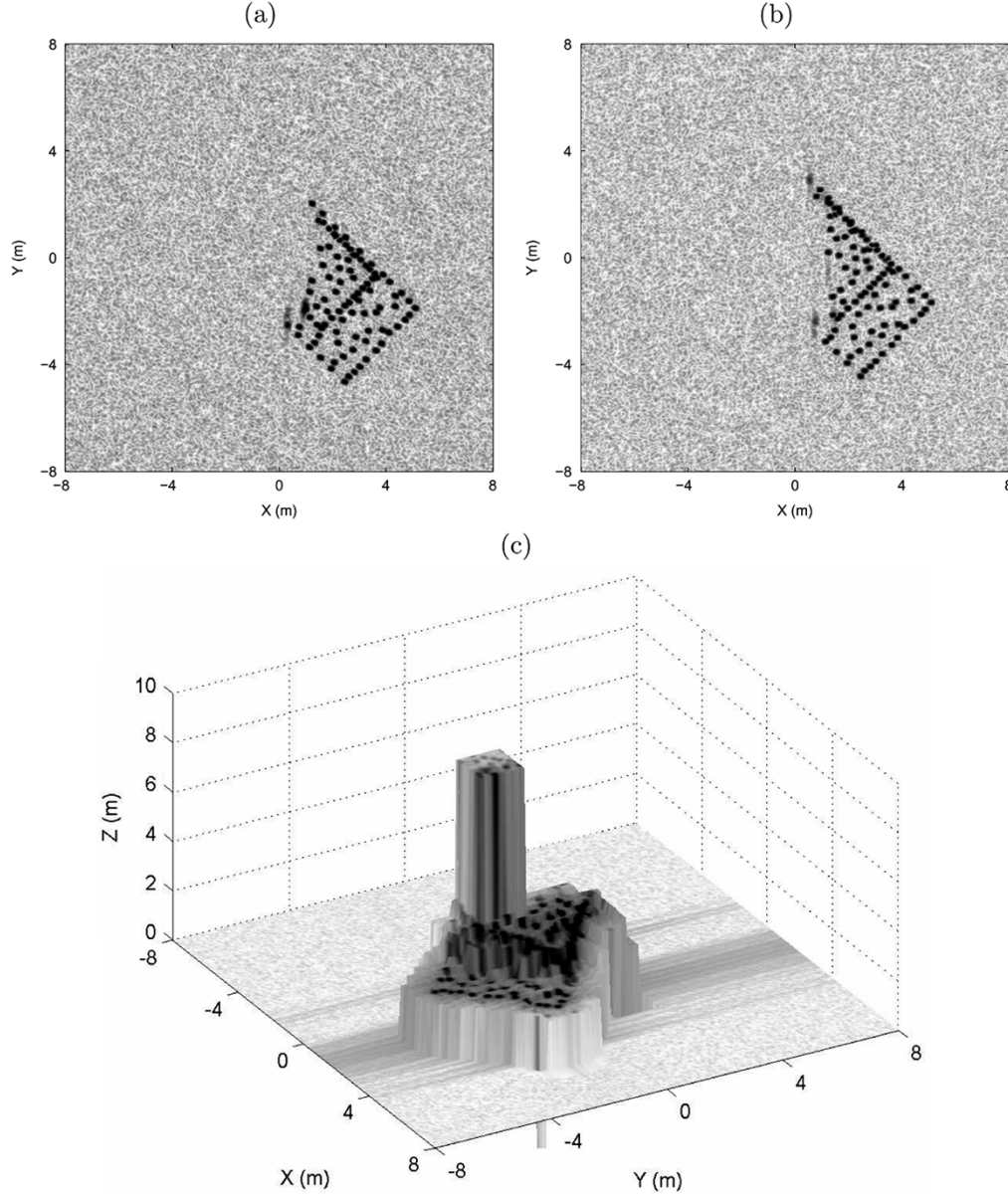
Fig. 4.   Transmitter aperture is centered at $\phi_t = 0°$. (a) Image formed by a receiver with aperture centered at $\phi_{r1} = -20°$. (b) Image formed by a receiver with aperture centered at $\phi_{r2} = 5°$. (c) Three-dimensional surface reconstruction formed from (a) and (b). Tightly spaced scatterers lay over onto the same image regions, thus hindering stereo height estimation.

and covariance K_{xy}, then, from (23), the variance of the relative height estimate is

$$\sigma_{z12}^2 = \frac{\underline{u}_z^T K_{xy} \underline{u}_z}{\|\underline{u}_z\|^4} \qquad (25)$$

where the unknown offset due to geolocation errors $\tilde{z}_{12}$ has been omitted. The strong dependence on imaging geometry is embodied in the $\|\underline{u}_z\|^4$ term in the denominator. The transmitter and receiver viewing angles determine the norm of $\underline{u}_z$, which is equal to the layover offset between two images of a scatterer with 1-m height, is defined in (22). The variance of the shift estimate errors (the diagonal elements of K_{xy}) will decrease with improved resolution and will increase with increasing clutter and noise powers in the image. The covariance K_{xy} can be written as

$$K_{xy} = \underline{e}_1 \underline{e}_1^T \sigma_{e1}^2 + \underline{e}_2 \underline{e}_2^T \sigma_{e2}^2 \qquad (26)$$

where σ_{e1}^2 is the variance of shift estimates in the $\underline{e}_1$ direction, and σ_{e2}^2 is the variance of shift estimates in the $\underline{e}_2$ direction. The unit vectors $\underline{e}_1$ and $\underline{e}_2$ correspond to nominal range and azimuth directions, such that σ_{e1}^2 and σ_{e2}^2 are related to range and azimuth resolution values. In images with square resolution cells, K_{xy} will be diagonal.

To test the above assertions, we synthesized multistatic phase history data for the return from a single point scatterer. The transmitting platform was located at $(\bar{\phi}_t, \bar{\theta}_t) = (0°, 20°)$, and the two receiving platforms were located at $(\bar{\phi}_{r1}, \bar{\theta}_{r1}) = (5°, 20°)$ and $(\bar{\phi}_{r2}, \bar{\theta}_{r2}) = (-20°, 20°)$, respectively. All three platforms viewed the scene at broadside.

In each of the 200 Monte Carlo simulations, two bistatic SAR images were formed, one corresponding to the phase history data from each receiver. Within each image, a point scatterer was randomly placed, and white Gaussian noise, commensu-
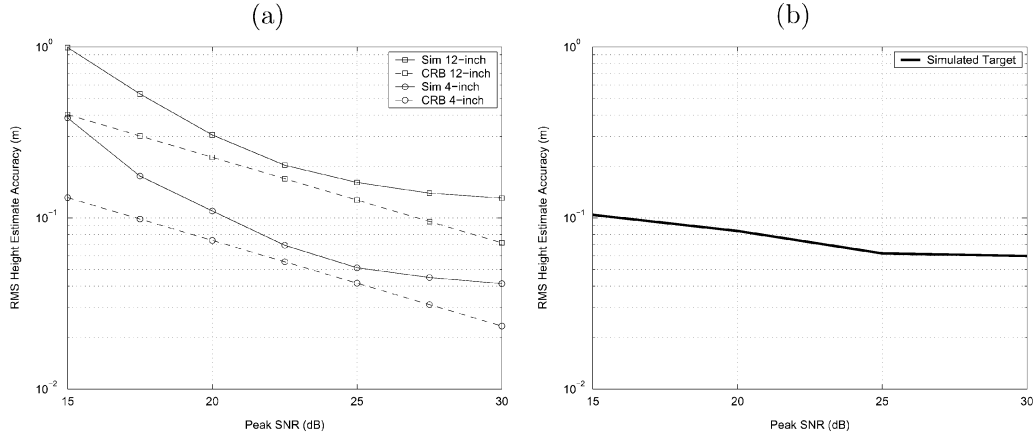
(a)

(b)

Fig. 5. (a) Predicted RMS accuracy of stereo height estimates (dotted lines) and observed RMS accuracy (solid lines) for a single, isolated point scatterer. Two radar image resolutions are considered. (b) Observed RMS height error for the example in Fig. 3, for various SNR values.

rate with the SNR under study, was added. The relative shift of the scatterer between images was then estimated and subtracted from the actual shift, to yield a shift estimate error. After all Monte Carlo simulations for a particular SNR and resolution had been completed, the ensemble of shift estimate errors was used to compute an estimate of K_{xy} in (26), which was then input to (25) to obtain an estimate of σ_{z12}^2. This value predicts the variance of height estimates from a pair of bistatic SAR images with a given SNR, a given resolution, and the described geometric configuration. Simulations were performed at SNRs ranging from 15-30 dB, and with 4-in (0.1 m) and 12-in (0.3 m) square Fourier resolution cells.

Fig. 5(a) (without the thick line) compares the σ_{z12}^2 computed via simulation to the accuracy predicted by an approximated Cramér–Rao lower bound (CRLB) [26]. The CRLB is a well-documented means for computing optimal achievable performance of unbiased estimators. The CRLB for a parametric model gives the minimum variance that an unbiased estimator of that model can achieve in the presence of additive noise under a given distribution. The details involved in deriving our approximation of the CRLB are given in the Appendix. For moderate SNR, the algorithm provides performance close to the CRLB. At low SNR, the algorithm deviates from the CRLB because of estimation errors in the correlation peak finding process. At high SNR, the deviation in algorithm performance is due to bias errors that result from using simple interpolation methods and images that are less than twice over sampled; generation of highly over-sampled images, and use of better interpolation methods in the peak-finding algorithm, would reduce the bias, at the expense of greater computational complexity.

Fig. 5(b) shows the RMS height accuracy values using the scenario from Fig. 3, but with differing SNR values. At each SNR, the RMS height error is computed over all of the detected scattering centers in the image. These results are not directly comparable to the simulation errors or bounds in Fig. 5(a), because, in this case, we have multiple scattering centers in each subimage. However, the observed performance for this complex scene has RMS height errors that are close to the CRLB prediction and simulation. We hypothesize that the lower RMS error at low SNR [compared to the CRLB in Fig. 5(a)] is due to a

boosted SNR in some subimages, resulting from multiple scattering centers in the same subimage. At higher SNR, we hypothesize that the higher RMS values in Fig. 5(b) are caused by interference between the multiple scattering centers in a subimage. Note that the results presented here represent a lower bound on predicted performance, as the simulated scene contained a single point scatterer.

V. COORDINATION STRATEGIES FOR MULTISTATIC SAR

The performance prediction framework developed in Section IV may be extended to consider the availability of more than two bistatic apertures. As each aperture will result in a scene shifted by that aperture's motion measurement errors, these geo-location errors add a new layer of complexity to the problem. Thus, for the remainder of our discussion, we will assume that all of the multistatic images produced by our system are perfectly registered; therefore, the shift observed between subimages from different apertures is solely due to the layover differences between those apertures. In Section IV, we demonstrated that the accuracy of stereo height estimates from a pair of bistatic apertures is dependent on the variance of relative shift estimates, via K_{xy} in (25).

Note that σ_{z12}^2 in (25) is inversely proportional to $\|\underline{u}_z\|^2$, indicating that adding geometric diversity to increase the norm of $\underline{u}_z$ will enhance the quality of height estimates. However, the variance expressed in (25) is based solely on the geometry of the respective bistatic apertures. It does not take into account variations in the visibility of scatterers in the scene and other scintillation effects. By viewing a given target from two bistatic look angles separated greatly enough in azimuth, one would naturally expect that the resultant images would be largely decorrelated, and, thus, it would be impossible to accurately measure a relative shift. Therefore, we propose a quality measure defined as

$$Q_{ij} = \frac{W(\bar{\phi}_{\mathrm{bi}} - \bar{\phi}_{\mathrm{bj}})}{\sigma_{zij}^2} \qquad (27)$$

where the quality of the height estimates obtained from the ith and jth images improves as Q_{ij} increases. The function
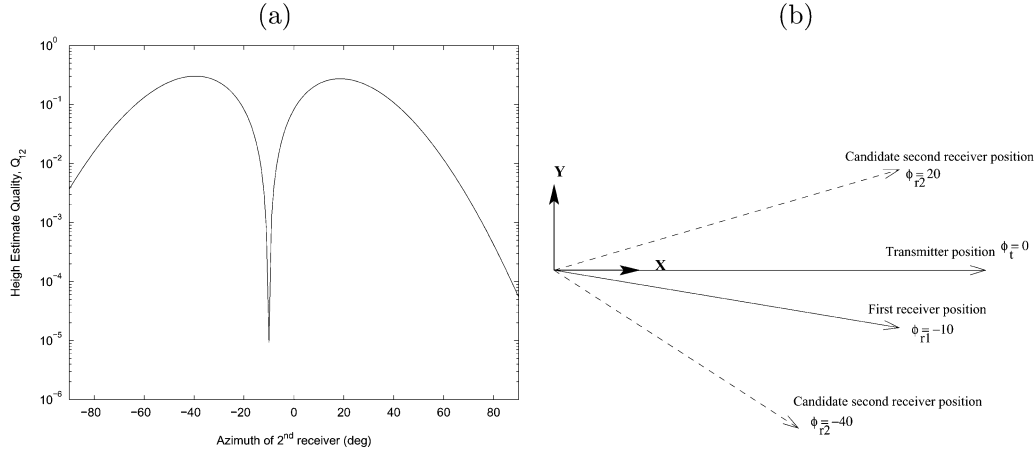
Fig. 6. (a) Height estimation quality of a two receiver multistatic system with transmitter at $\phi_t = 0°$ azimuth and first receiver at $\phi_{r1} = -10°$ azimuth, as a function of the location of the second receiver. (b) Positioning the second receiver at $\phi_{r2} = -40°$ or $\phi_{r2} = 20°$ gives the best predicted height estimation quality.

$W(\bar{\phi}_{\mathrm{bi}} - \bar{\phi}_{\mathrm{bj}})$ models the degree to which images formed from two given bistatic look angles are correlated. The variables $\bar{\phi}_{\mathrm{bi}}$ and $\bar{\phi}_{\mathrm{bj}}$ are the bistatic look angles of the ith and jth apertures. Zebker and Villasenor propose a triangular model for image decorrelation in [27]

$$W(\bar{\phi}_{\mathrm{bi}} - \bar{\phi}_{\mathrm{bj}}) = 1 - \frac{|\bar{\phi}_{\mathrm{bi}} - \bar{\phi}_{\mathrm{bj}}|}{a} \quad \text{for } |\bar{\phi}_{\mathrm{bi}} - \bar{\phi}_{\mathrm{bj}}| < a. \quad (28)$$

In our experiments, we found that the above model and a Gaussian model, which is more easily implemented in simulation software and gives a more intuitive result

$$W(\bar{\phi}_{\mathrm{bi}} - \bar{\phi}_{\mathrm{bj}}) = \exp\left\{ -2 \frac{\left(\bar{\phi}_{\mathrm{bi}} - \bar{\phi}_{\mathrm{bj}}\right)^2}{a^2} \right\} \quad (29)$$

behaved similarly.

The quality metric given in (27) may also be applied to multistatic scenarios involving more than a pair of bistatic apertures. Before evaluating the accuracy of height estimates from such multistatic systems, we must define a means of estimation. One simple method of computing a height estimate from multistatic measurements is to first compute a height estimate from each of the possible pairings of apertures and then to linearly combine these estimates. The number of possible pairings in a system consisting of N_{ap} apertures is $\binom{N_{\mathrm{ap}}}{2}$. Based on the parameters of each pair of apertures, one may use the methods of Section IV to compute a height estimate $\hat{z}_{ij}^{(m)}$ from the ith and jth apertures and to compute a variance σ_{zij}^2 for that estimate. A linear estimator of the true height, given independent estimates, may then be calculated as

$$\hat{z}^{(m)} = \frac{\sum_{i=1}^{N_{\mathrm{ap}}-1} \sum_{j=i+1}^{N_{\mathrm{ap}}} \hat{z}_{ij}^{(m)} \sigma_{zij}^{-2}}{\sum_{i=1}^{N_{\mathrm{ap}}-1} \sum_{j=i+1}^{N_{\mathrm{ap}}} \sigma_{zij}^{-2}} \quad (30)$$

and the quality of this aggregate estimate is computed as

$$Q = \left(\sum_{i=1}^{N_{\mathrm{ap}}-1} \sum_{j=i+1}^{N_{\mathrm{ap}}} W(\bar{\phi}_{\mathrm{bi}} - \bar{\phi}_{\mathrm{bj}}) \sigma_{zij}^{-2} \right)^{-1} . \quad (31)$$

In actuality, the estimates $\hat{z}_{ij}^{(m)}$ will be correlated to some degree, depending on the azimuth spacing of the bistatic apertures. This implies (31) will function as an upper bound on the achievable height estimate quality.

Using (31) as a metric for predicted performance, with σ_{zij}^2 defined by (25), we may propose strategies for coordinating multistatic systems. We first consider an example requiring placement of a second receiver, given the location of the transmitter and the first receiver, such that the height estimation quality Q_{12} is maximized. We assume a Gaussian decorrelation model, as in (29), with a spread of $a = 20°$. The transmitter is located at $\phi_t = 0°$, and the first receiver is located at $\phi_{r1} = -10°$. The transmitter and receivers view the scene at broadside, and the elevation angles of the receivers and the transmitter are fixed at $20°$. Fig. 6(a) shows the height estimation quality, computed using (27), as a function of the azimuth location of the second receiver. As one might expect, the height estimation accuracy at first improves as the receiver separation increases; however, the scene decorrelation model eventually begins to dominate and worsens the predicted performance. As shown in Fig. 6(b), positioning the second receiver at $\phi_{r2} = -40°$ or $\phi_{r2} = 20°$ gives the best predicted height estimation quality.

As a second example, we add a third receiver to the scenario of the first example. Now, two receivers with identical and fixed elevation angles must be placed in azimuth in order to best complement each other and the original receiver. Fig. 7(a) and (b) shows the height estimation quality Q, computed using (29) and (31), as a function of the azimuth locations of the two added receivers. Fig. 7(c) and (d) shows two candidate receiver configurations that are predicted to give high-quality height estimation. The peaks of this plot are consistent with maintaining roughly $20°$ separation between receivers and alternating which of the three receivers is in the middle.

VI. Conclusion

In this paper, we generalized the theory behind monostatic stereo processing and interferometric processing of SAR images, in order to develop 3-D surface reconstruction algorithms
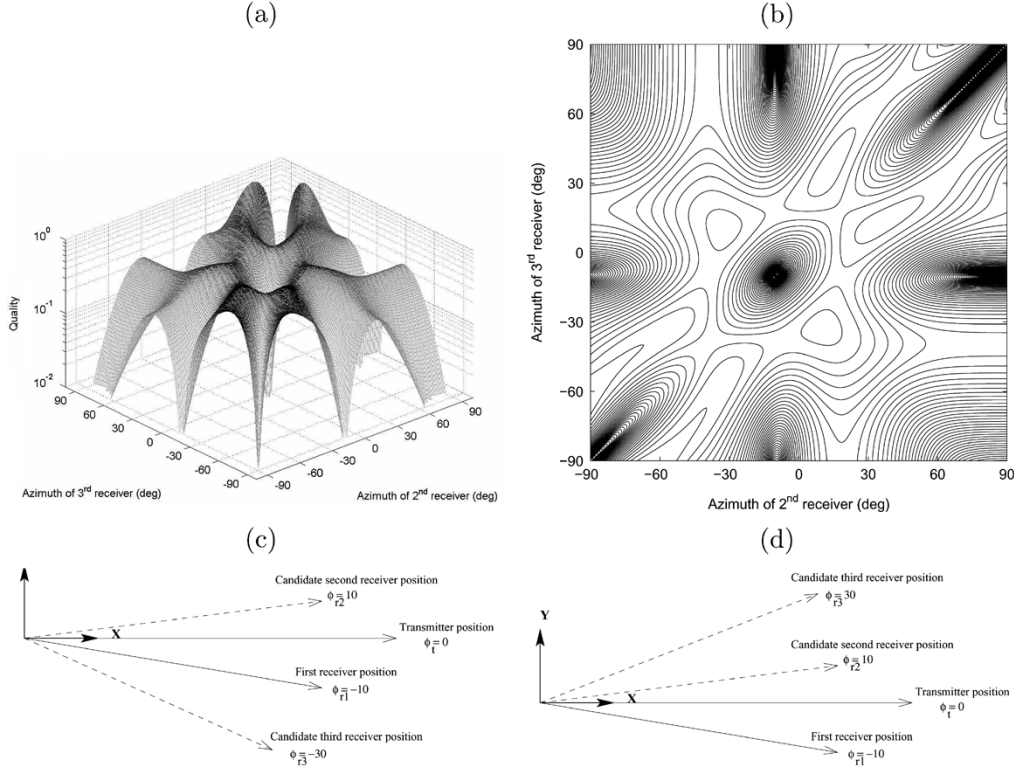
(a)

(b)

(c)

(d)

Fig. 7. (a) and (b) Height estimation quality of a three receiver multistatic system with transmitter at $\phi_t = 0°$ azimuth and first receiver at $\phi_{r1} = -10°$ azimuth, as a function of the location of the second and third receivers. (c) and (d) Two candidate receiver configurations that are predicted to give high-quality height estimates.

for multistatic SAR systems. As in earlier treatments of interferometric processing, estimation of surface heights from a pair of bistatic SAR images on a pixel-by-pixel basis is highly sensitive to the SNR and scintillation of individual scattering centers. While stereo SAR is more robust with respect to SNR, it relies heavily on the assumption that scatterers will be observable by multiple synthetic apertures. In an attempt to capture this effect, we proposed a height estimate quality metric, dependent on both geometric diversity and image decorrelation. Future work will necessarily involve further development of this performance prediction theory and development of algorithms for accurate and efficient subimage shift estimation. One might also further study the effect of SNR and resolution on stereo and interferometric height estimation accuracy.

APPENDIX
DERIVATION OF THE CRLBs ON THE VARIANCE OF 3-D SCATTERER POSITION ESTIMATES FROM BISTATIC STEREO SAR DATA

The method for computing a CRLB, as detailed in [26], is as follows. First, one must construct the Fisher's information (FI) matrix for the given parametric model and noise distribution. A FI matrix is square with number of rows equal to the number of parameters in the model. The elements of this matrix are defined as

$$F_{pq} = E\left\{\left(\frac{\partial \log p(Y \mid \underline{\Theta})}{\partial \theta_p}\right)^T \left(\frac{\partial \log p(Y \mid \underline{\Theta})}{\partial \theta_q}\right)\right\} \quad (32)$$

where $E\{\cdot\}$ represents the expected value, $\theta_p \in \Theta$ is the pth model parameter, and $\log(p(Y \mid \underline{\Theta}))$ is the log-likelihood function of the observed random signal Y given the parameter vector $\underline{\Theta}$. Once the FI matrix has been constructed, the CRLB is found as the inverse of the FI matrix. The diagonal entries of the CRLB are the minimum achievable variances for any unbiased estimator of these parameters under the given noise conditions. By using the CRLB, one can predict the efficacy of a parametric model under noisy conditions and, in our case, at a given resolution.

Simulated bistatic SAR images of a single point scatterer, used in the Monte Carlo simulations of Section IV-C, are well approximated by analytically computing an approximation of the matched filter in (3) (see, e.g., [21]) to give

$$\begin{aligned}
&s_i(x, y; A_i, \psi_i, x_i, y_i) \\
&= A_i e^{j\psi_i} \frac{\sin\left[\frac{2\pi B_x}{c}((x - x_i)\cos\bar{\phi}_{\text{bi}} + (y - y_i)\sin\bar{\phi}_{\text{bi}})\right]}{\sin\left[\frac{2\pi B_x}{cN_x}((x - x_i)\cos\bar{\phi}_{\text{bi}} + (y - y_i)\sin\bar{\phi}_{\text{bi}})\right]} \\
&\quad \cdot \frac{\sin\left[\frac{2\pi B_y}{c}((x - x_i)\sin\bar{\phi}_{\text{bi}} - (y - y_i)\cos\bar{\phi}_{\text{bi}})\right]}{\sin\left[\frac{2\pi B_y}{cN_y}((x - x_i)\sin\bar{\phi}_{\text{bi}} - (y - y_i)\cos\bar{\phi}_{\text{bi}})\right]} \\
&\quad + w_i(x, y), \quad i = 1, 2
\end{aligned} \quad (33)$$

where $\bar{\phi}_{\text{bi}}$ is the bistatic SAR look angle of the ith receiver, and $w_i(x, y)$ is circular white Gaussian noise with zero mean and variance σ^2. The amplitude and phase of the scatterer are given by A_i and ψ_i, respectively. The laid over position of a scatterer, with 3-D location (x_m, y_m, z_m), in the ith image is

$[x_i \; y_i]^T = P_i Q_i [x_m \; y_m \; z_m]^T$. The image is assumed to be supported by spatial frequency data in x and y with N_x and N_y samples over bandwidths B_x and B_y, respectively. The amplitude of (33) has a Rician distribution, which is intractable for CRLB analysis. However, at high SNR, a Rician distribution [28] is well approximated by a Gaussian. This allows approximation of the amplitude of (33) with

$$
\begin{aligned}
&s_i(x, y; A_i, x_i, y_i)\\
&= A_i \left| \frac{\sin\left[\frac{2\pi B_x}{c}((x-x_i)\cos\bar{\phi}_{\text{bi}} + (y-y_i)\sin\bar{\phi}_{\text{bi}})\right]}{\sin\left[\frac{2\pi B_x}{cN_x}((x-x_i)\cos\bar{\phi}_{\text{bi}} + (y-y_i)\sin\bar{\phi}_{\text{bi}})\right]} \right. \\
&\left. \cdot \frac{\sin\left[\frac{2\pi B_y}{c}((x-x_i)\sin\bar{\phi}_{\text{bi}} - (y-y_i)\cos\bar{\phi}_{\text{bi}})\right]}{\sin\left[\frac{2\pi B_y}{cN_y}((x-x_i)\sin\bar{\phi}_{\text{bi}} - (y-y_i)\cos\bar{\phi}_{\text{bi}})\right]} \right| \\
&\quad + v_i(x, y), \quad i = 1, 2
\end{aligned}
\tag{34}
$$

where $v_i(x, y)$ is assumed to be white Gaussian with zero mean and variance $\sigma^2/2$.

We now wish to compute a lower bound on the variance of estimates of the parameters $\theta_p \in \underline{\Theta} = \{A_1, A_2, x_m, y_m, z_m\}$ from the aggregate data set $y = [s_1(x, y; A_1, x_1, y_1) \; s_2(x, y; A_2, x_2, y_2)]$. For convenience, we define the dummy variable $s(\underline{\Theta}) = y - [v_1(x, y) \; v_2(x, y)]$, and we reformat the data such that y and $s(\underline{\Theta})$ are one-dimensional vectors of length $N = N_x N_y$. Thus, the likelihood function for y is

$$
p(y \,|\, \underline{\Theta}) = \frac{1}{(\pi\sigma^2)^{N/2}} \exp\left(-\frac{(y - s(\underline{\Theta}))^T (y - s(\underline{\Theta}))}{\sigma^2} \right)
\tag{35}
$$

and the log-likelihood function is

$$
\log p(y \,|\, \underline{\Theta}) = -\frac{N}{2} \log(\pi\sigma^2) - \frac{1}{\sigma^2}(y - s(\underline{\Theta}))^T (y - s(\underline{\Theta}))
\tag{36}
$$

where y is a noisy realization of the signal with mean $s(\underline{\Theta})$ and variance of $\sigma^2/2$ on each frequency sample. Taking the derivatives of our log-likelihood function with respect to $\theta_p \in \underline{\Theta} = \{A_1, A_2, x_m, y_m, z_m\}$ yields

$$
\frac{\partial \log p(y \,|\, \underline{\Theta})}{\partial \theta_p} = \frac{2}{\sigma^2}(y - s(\underline{\Theta}))^T \left(\frac{\partial s(\underline{\Theta})}{\partial \theta_p} \right)
\tag{37}
$$

which can be computed for each element of $\underline{\Theta}$. Next, we compute each entry of the Fisher matrix

$$
\begin{aligned}
F_{pq} &= E\left\{ \left(\frac{\partial \log p(y \,|\, \underline{\Theta})}{\partial \theta_p} \right)^T \left(\frac{\partial \log p(y \,|\, \underline{\Theta})}{\partial \theta_q} \right) \right\} \\
&= \frac{4}{\sigma^4} \left(\frac{\partial s(\underline{\Theta})}{\partial \theta_p} \right)^T E\{(y - s(\underline{\Theta}))(y - s(\underline{\Theta}))^T\}) \left(\frac{\partial s(\underline{\Theta})}{\partial \theta_q} \right) \\
&= \frac{2}{\sigma^2} \left(\frac{\partial s(\underline{\Theta})}{\partial \theta_p} \right)^T \left(\frac{\partial s(\underline{\Theta})}{\partial \theta_q} \right).
\end{aligned}
\tag{38}
$$

The derivatives for the model of (34) with respect to $\theta_p \in \underline{\Theta} = \{A_1, A_2, x_m, y_m, z_m\}$ may be computed analytically or numerically. Finally, the CRLB of our parameter set is defined to be

the inverse of the Fisher matrix, $C_{\underline{\Theta}} = F^{-1}$; the lower bound on the variance of each parameter is given by the corresponding diagonal element of F^{-1}, such that $\text{var}(\theta_{ii}) \geq [C_{\underline{\Theta}}]_{ii}$.

REFERENCES

[1] L. Cazzani *et al.*, "A ground based parasitic SAR experiment," in *Proc. IEEE IGARSS*, vol. 3, 1999, pp. 1525–1527.

[2] H. M. Jones, "Predicted properties of bistatic satellite images," in *Proc. IEEE Nat. Radar Conf.*, Apr. 1993, pp. 286–291.

[3] G. P. Cardillo, "On the use of the gradient to determine bistatic SAR resolution," in *Proc. Antennas Propagation Soc. Int. Symp.*, vol. 2, May 1990, pp. 1032–1035.

[4] Y. Wu and D. C. Munson, "Wide-angle ISAR passive imaging using smoothed pseudo Wigner-Ville distribution," in *Proc. IEEE Radar Conf.*, 2001, pp. 363–368.

[5] J. Detlefsen, "Application of multistatic radar principles to shortrange imaging," *Proc. Inst. Elect. Eng.*, vol. 133, no. 7, pp. 658–663, Dec. 1986.

[6] C. Mikhail, K. Kurt, and N. David, "Bistatic synthetic aperture radar with noncooperative LEOS based transmitter," in *Proc. IEEE Int. Geoscience and Remote Sensing Symp.*, vol. 2, 2000, pp. 861–862.

[7] A. M. Horne and G. Yates, "Bistatic synthetic aperture radar," *Proc. IEE Radar*, pp. 6–10, Oct. 2002.

[8] M. Lowe, "Algorithms for high resolution bistatic SAR," *Proc. IEE Radar*, pp. 512–515, Oct. 2002.

[9] O. Arikan and D. C. Munson, "A tomographic formulation of bistatic synthetic aperture radar," in *Proc. ComCon*, Oct. 1988, p. 418.

[10] A. D. M. Garvin and M. R. Inggs, "Use of synthetic aperture and stepped-frequency continuous wave processing to obtain radar images," in *Proc. South African Symp. Communications and Signal Processing*, 1991, pp. 32–35.

[11] M. Soumekh, "Bistatic synthetic aperture radar inversion with application in dynamic object imaging," *IEEE Trans. Signal Process.*, vol. 39, no. 9, pp. 2044–2055, Sep. 1991.

[12] B. D. Rigling and R. L. Moses, "Polar format algorithm for bistatic SAR," *IEEE Trans. Aerosp. Electron. Syst.*, to be published.

[13] M. Soumekh, "Multistatic echo imaging in remote sensing and diagnostic medicine," presented at the 6th Multidimensional Signal Processing Workshop, 1989.

[14] L. C. Graham, "Synthetic interferometer radar for topographic mapping," *Proc. IEEE*, vol. 62, no. 6, pp. 763–768, Jun. 1974.

[15] H. Zebker and R. Goldstein, "Topographic mapping from interferometric SAR observations," *J. Geophys. Res.*, vol. 91, pp. 4993–4999, 1986.

[16] A. K. Gabriel and R. M. Goldstein, "Crossed orbit interferometry: Theory and experimental results from SIR-B," *Int. J. Remote Sens.*, vol. 9, pp. 857–872, 1988.

[17] M. D. Desai, "Spotlight mode SAR stereo technique for height computation," *IEEE Trans. Image Process.*, vol. 6, no. 12, pp. 1400–1411, Dec. 1997.

[18] C. V. Jakowatz Jr., D. E. Wahl, and P. A. Thompson, "Threedimensional SAR imaging using cross-track coherent stereo collections," in *Proc. 31st Asilomar Conf. Signals, Systems, Computers*, vol. 2, 1997, pp. 1199–1203.

[19] W. G. Carrara, R. S. Goodman, and R. M. Majewski, *Spotlight Synthetic Aperture Radar: Signal Processing Algorithms*. Norwood, MA: Artech House, 1995.

[20] C. V. Jakowatz, D. E. Wahl, and P. H. Eichel, *Spotlight-Mode Synthetic Aperture Radar: A Signal Processing Approach*. Boston, MA: Kluwer, 1996.

[21] B. Rigling, "Signal processing strategies for bistatic synthetic aperture radar," Ph.D. dissertation, Dept. Elect. Eng., The Ohio State Univ., Columbus, 2003.

[22] B. D. Rigling and R. L. Moses, "Motion measurement errors and autofocus in bistatic SAR," *IEEE Trans. Image Process.*, to be published.

[23] E. Rodriguez and J. M. Martin, "Theory and design of interferometric synthetic aperture radars," *Proc. Inst. Elect. Eng.*, vol. 139, no. 2, pp. 147–159, Apr. 1992.

[24] D. Just and R. Bamler, "Phase statistics of interferograms with applications to synthetic aperture radar," *Appl. Opt.*, vol. 33, no. 20, pp. 4361–4368, Jul. 1994.

[25] G. Minkler and J. Minkler, *CFAR: The Principles of Automatic Radar Detection in Clutter*. Baltimore, MD: Magellan, 1990.

[26] H. L. Van Trees, *Detection, Estimation, and Modulation Theory Part I*. New York: Wiley, 1968.

[27] H. A. Zebker and J. Villasenor, "Decorrelation in interferometric radar echoes," *IEEE Trans. Geosci. Remote Sens.*, vol. 30, no. 5, pp. 950–959, Sep. 1992.

[28] H. Stark and J. W. Woods, *Probability, Random Processes, and Estimation Theory for Engineers*. Upper Saddle River, NJ: Prentice-Hall, 1994.

Brian D. Rigling (S'00–M'03) received the B.S. degree in physics-computer science from the University of Dayton, Dayton, OH, in 1998 and the M.S. and Ph.D. degrees in electrical engineering from The Ohio State University, Columbus, in 2000 and 2003, respectively.

Since July 2004, he has been with the Department of Electrical Engineering, Wright State University, Dayton, where he is currently an Assistant Professor. From 2000 to 2004, he was a Radar Systems Engineer for Northrop Grumman Electronic Systems, Baltimore, MD. His research interests are in sensor signal processing and system engineering, array processing, autofocus, parametric modeling, and estimation.

Randolph L. Moses (S'78–M'85–SM'90) received the B.S., M.S., and Ph.D. degrees in electrical engineering from Virginia Polytechnic Institute and State University, Blacksburg, in 1979, 1980, and 1984, respectively.

Since 1985, he has been with the Department of Electrical Engineering, The Ohio State University, Columbus, where he is currently a Professor. During the summer of 1983, he was a Summer Faculty Research Fellow, Rome Air Development Center, Rome, NY. From 1984 to 1985, he was a NATO Postdoctoral Fellow, Eindhoven University of Technology, Eindhoven, The Netherlands. From 1994 to 1995, he was on sabbatical leave at Uppsala University, Uppsala, Sweden, and from 2002 to 2003, he was on sabbatical leave at the Air Force Research Laboratory, Dayton, OH, and at the Massachusetts Institute of Technology, Cambridge. He is the coauthor, with P. Stoica, of *Introduction to Spectral Analysis* (Upper Saddle River, NJ: Prentice-Hall, 1997). His research interests are in stochastic signal processing and include parametric estimation, array signal processing, sensor networks, and radar imaging.

Dr. Moses is a member of Eta Kappa Nu, Tau Beta Pi, Phi Kappa Phi, and Sigma Xi. He served as an Associate Editor for the IEEE TRANSACTIONS ON SIGNAL PROCESSING from 2001 to 2004, and he served on the IEEE Signal Processing Society Technical Committee on Statistical Signal and Array Processing from 1991 to 1994.